

## RESEARCH ARTICLE

10.1002/2013WR013673

### Key Points:

- First quantitative analysis of transient fingering using field data and modeling
- Geophysics and modeling agree on timing and concentration of convective fingers
- Fingering was caused by infiltration of a precipitation-induced brine

### Correspondence to:

R. L. Van Dam,  
rvd@msu.edu

### Citation:

Van Dam, R. L., B. P. Eustice, D. W. Hyndman, W. W. Wood, and C. T. Simmons (2014), Electrical imaging and fluid modeling of convective fingering in a shallow water-table aquifer, *Water Resour. Res.*, 50, 954–968, doi:10.1002/2013WR013673.

Received 18 FEB 2013

Accepted 28 DEC 2013

Accepted article online 4 JAN 2014

Published online 6 FEB 2014

## Electrical imaging and fluid modeling of convective fingering in a shallow water-table aquifer

Remke L. Van Dam<sup>1,2</sup>, Brian P. Eustice<sup>1,3</sup>, David W. Hyndman<sup>1</sup>, Warren W. Wood<sup>1</sup>, and Craig T. Simmons<sup>4</sup>

<sup>1</sup>Department of Geological Sciences, Michigan State University, East Lansing, Michigan, USA, <sup>2</sup>Science and Engineering Faculty, Institute for Future Environments, Queensland University of Technology, Brisbane, Queensland, Australia, <sup>3</sup>Now at Golder Associates, Lansing, Michigan, USA, <sup>4</sup>National Centre for Groundwater Research and Training, School of the Environment, Flinders University, Adelaide, South Australia, Australia

**Abstract** Unstable density-driven flow can lead to enhanced solute transport in groundwater. Only recently has the complex fingering pattern associated with free convection been documented in field settings. Electrical resistivity (ER) tomography has been used to capture a snapshot of convective instabilities at a single point in time, but a thorough transient analysis is still lacking in the literature. We present the results of a 2 year experimental study at a shallow aquifer in the United Arab Emirates that was designed to specifically explore the transient nature of free convection. ER tomography data documented the presence of convective fingers following a significant rainfall event. We demonstrate that the complex fingering pattern had completely disappeared a year after the rainfall event. The observation is supported by an analysis of the aquifer halite budget and hydrodynamic modeling of the transient character of the fingering instabilities. Modeling results show that the transient dynamics of the gravitational instabilities (their initial development, infiltration into the underlying lower-density groundwater, and subsequent decay) are in agreement with the timing observed in the time-lapse ER measurements. All experimental observations and modeling results are consistent with the hypothesis that a dense brine that infiltrated into the aquifer from a surficial source was the cause of free convection at this site, and that the finite nature of the dense brine source and dispersive mixing led to the decay of instabilities with time. This study highlights the importance of the transience of free convection phenomena and suggests that these processes are more rapid than was previously understood.

### 1. Introduction

Free convection, fluid motion driven by density differences, is an important mechanism for transport and mixing of heat and solutes in the subsurface. The relevance of this process has long been recognized and studied by the hydrology community. Most research in this area has focused on deep subsurface and geothermal phenomena [e.g., *Garven et al.*, 1999; *Yang et al.*, 2004; *Coumou et al.*, 2008]. Numerous issues of environmental and societal relevance are exacerbated by mixing due to density-driven flow including contaminant plumes with higher densities than the background fluid [e.g., *Schincariol and Schwartz*, 1990; *Koch and Zhang*, 1992; *Zhang and Schwartz*, 1995; *Liu and Dane*, 1996; *Fan et al.*, 1997; *Nield et al.*, 2008]. Density-driven flow in groundwater has also been studied in the context of nuclear waste disposal [*Yang and Edwards*, 2000], hydrothermal springs [*Cardenas et al.*, 2012], greenhouse gas sequestration in deep formations [*Riaz et al.*, 2006; *Hidalgo and Carrera*, 2009], sea level rise, and the impacts of saline intrusion on drinking water resources [*Kooi et al.*, 2000; *Hodgkinson et al.*, 2007]. Extensive reviews on the topic are given by *Simmons et al.* [2001], *Diersch and Kolditz* [2002], and *Nield and Bejan* [2006].

The basic theory behind unstable convective motion in porous media is well understood, especially for homogeneous, isotropic systems. In these settings, instabilities may develop when significant contrasts in fluid density exist due to differences in solute concentrations or temperatures. When the critical condition for the onset of free convection is exceeded, initial small-scale instabilities develop and then coalesce into larger fingers. Despite the importance of free convection in a wide range of fields within and outside the hydrologic sciences, important questions regarding this process in natural systems remain unanswered [*Simmons*, 2005]. These questions include the unknown scalability of experimental results, the relative importance of various simplifications that are made to model systems with unstable fingering, and the

difficulty of relying on typical field observations of “equivalent freshwater head” to infer the existence of free convection. Even in nearly homogeneous and isotropic media, numerical simulation is complicated by the multidimensionality and temporal scales of the different processes, the initial and boundary conditions, the choice of spatial discretization, and uncertainty about hydrodynamic variables (e.g., the effect of the lateral diffusion and dispersion rate on the downward convective flow). In addition, spatial and temporal measurements of solute and temperature variations, which both influence density, are generally sparse.

Although there are thousands of published studies on free convection, almost all of these focus on either theory or modeling. Very few papers discuss experimental studies and even fewer have field measurements. Most published field studies only present single snapshots, and thus, transient changes in these systems have not been quantified. The rate of natural free convection in field settings is critical to reconcile measurements with theory and to improve numerical models that represent this process. Quantification of free convection in natural settings has remained elusive because it is difficult to directly document this process in the field. However, noninvasive electrical resistivity (ER) geophysical methods have the potential to exploit the relation between solute concentrations and electrical conductance of a fluid, thereby estimating fluid salinity differences in time and space. Indeed, ER has been used to document snapshots of complex fingering in field settings [Bauer *et al.*, 2006; Zimmermann *et al.*, 2006; Van Dam *et al.*, 2009].

Wood *et al.* [2002] suggested that density-driven convective flow was taking place in a sabkha (“salt flat” in Arabic) in the United Arab Emirates (UAE) based on measured density inversions and a distribution of elements (in particular tritium) consistent with vertical convective mixing. This could be explained by either episodic dissolution and infiltration of the halite crust or slow upwelling of lower-density water from lower formations. The UAE sabkha is an ideal natural laboratory for the study of free convection in a field setting because the sands are nearly homogeneous, meaning that measured ER differences will be almost entirely due to variations in solute concentration. Van Dam *et al.* [2009] used ER imaging to map the subsurface resistivity distribution in 2-D but did not include any numerical modeling or time-lapse measurements to assess temporal evolution of the fingers. Studies that combine field characterization of the transient process of fingering with numerical modeling are essential to reconcile theory and modeling efforts with an understanding of this process in the field.

Although ER has been previously used in a time-lapse study at a site with free convection [Stevens *et al.*, 2009], the 3-D resistivity models in that paper did not display clear fingers. Also, there was no specific attempt to quantify the fingering speeds. In this paper, we present the results of a 2-year study at the UAE field site of Van Dam *et al.* [2009], to characterize the persistence and transient nature of the convective fingering previously observed at the site; we also examine two conceptual models associated with free convection at this site. For this purpose, we analyzed ER data sets collected in 2008 and 2009 and conducted hydrodynamic modeling of the system. The time-lapse ER data allowed us to assess the persistence of complex fingering patterns observed in 2008, whereas the flow and transport simulations allowed us to study transient convective processes with more detail in space and time. The combination of both methods enabled an improved quantitative description of transient free convection.

## 2. Field Site Characterization

The study site is a sabkha located about 50 km southwest of the city of Abu Dhabi along the coast of the Arabian (Persian) Gulf in the United Arab Emirates, just landward of a series of parallel superficial beach ridges that indicate ongoing uplift in the region [Wood *et al.*, 2012] (Figure 1). A sabkha is a surface where evaporating groundwater results in precipitation of highly soluble halite, sylvite, and other minerals on the surface. Authigenic minerals including gypsum, anhydrite, calcite, and dolomite also form in the capillary zone. The sabkha topography is flat, with a gradient of  $\sim 1$  m per 6 km toward the coast [Wood *et al.*, 2012]. The study site consists of  $\sim 10$  m of homogeneous sand from reworked aeolian dunes deposited during Holocene sea level rise, with minor tidal clays near the surface [Eustice, 2011]. These sands of the Abu Dhabi Formation are underlain by the Gachsaran Formation, a Miocene carbonate.

The lateral water flux through the sabkha is calculated using Darcy’s law. Using a single-ring falling-head permeameter, we measured the hydraulic conductivity of the sabkha sand to be around 6.6 m/d, which is within an order of magnitude of the 1 m/d obtained from pumping tests on similar sediment [Sanford and Wood, 2001]. Using the regional hydraulic gradient of 0.0002 [Sanford and Wood, 2001], and assuming the

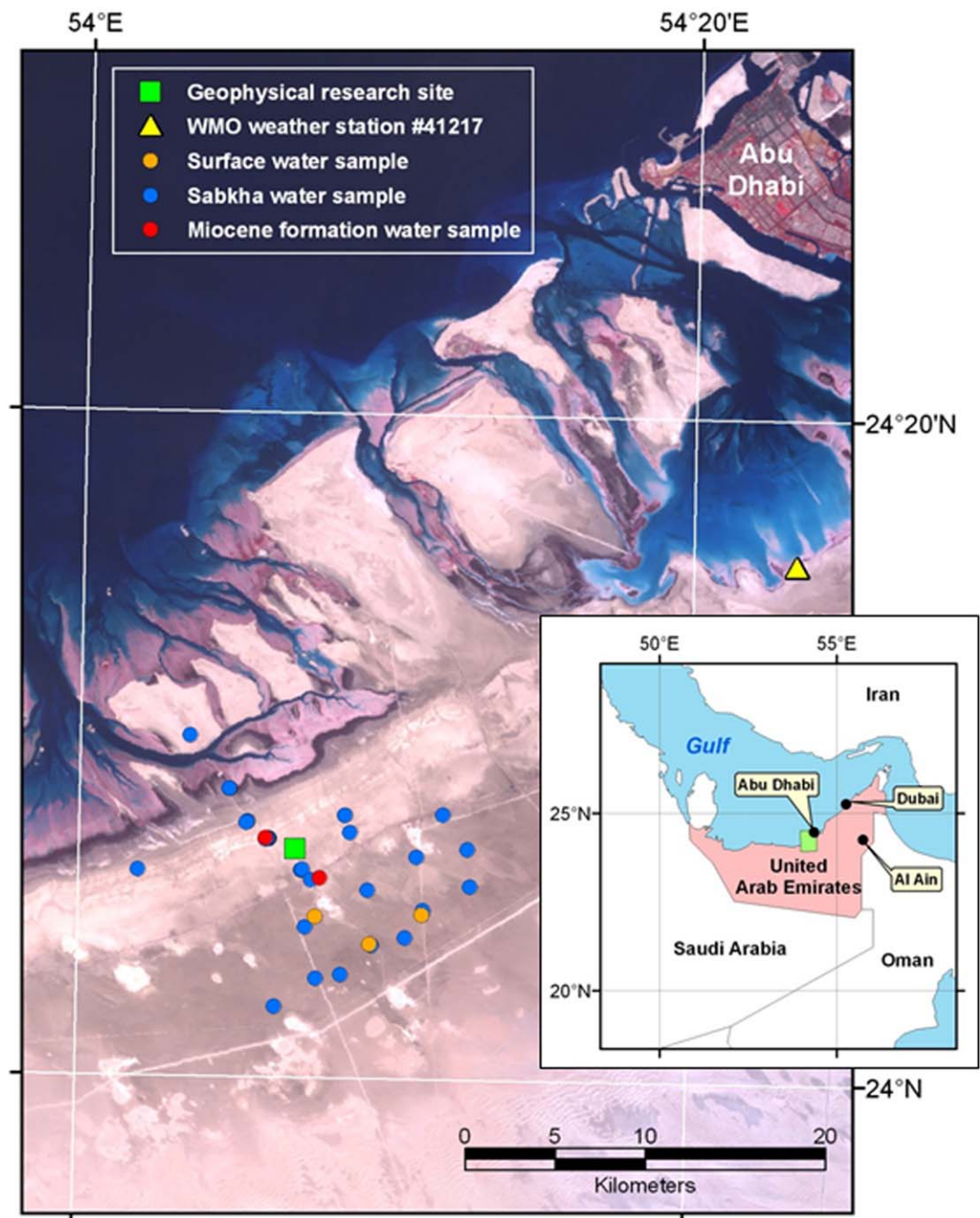


**Figure 1.** Location of the geophysical research site in relation to well and sample locations and the weather station (modified from Van Dam et al. [2009]). The inset shows location of the study area in the United Arab Emirates.

sediment is isotropic, the lateral flux is estimated to be 0.5 m/yr. Dividing this by the porosity (0.38) of the aquifer, the lateral seepage velocity is approximately 1.3 m/yr.

The UAE is a hot arid subtropical desert with mean minimum and maximum annual temperatures of 21.7 and 33°C, respectively. A long-term record (1983–2010) from a World Meteorological Organization, Geneva (WMO) weather station near the study site indicates an average annual rainfall of ~32 mm/yr, mostly from November to April. The mean annual rainfall has a large standard deviation since it is common to see multiple years with little rain (Figure 2). The pan evaporation rate of fresh water in the area is ~3500 mm/yr [Bottomley, 1996]. However, evaporation rates from the surface of the sabkha have been found to be less than

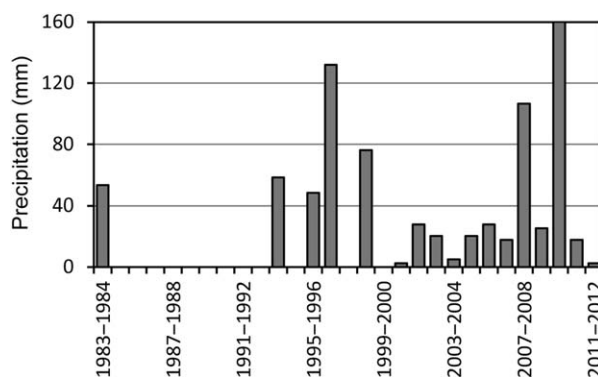


**Figure 2.** Annual rainfall based on hydrological year (1 October to 30 September) from 1983 to 2012 from WMO Weather Station 41217 near Abu Dhabi. More detailed information about rain events and sampling periods is shown in Figure 3.

3% of pan evaporation due to the reduced surface evaporation area associated with sediments, sealing of the surface with evaporates, and the high salt concentrations of water in the sabkha [Sanford and Wood, 2001]. Transpiration does not occur since there is no vegetation on the sabkha.

**2.1. Fluid Chemistry and Solute Mass Balance**

The chemistry of the water in the study area was characterized using a series of wells in the sabkha aquifer and underlying Gachsaran Formation [Wood et al., 2002; Wood, 2011]. Based on samples in a 10 km radius around the field site (Figure 1), the water in the sabkha (Abu

Dhabi Formation) aquifer was found to have an average solute concentration (total dissolved solids (TDS)) of 275.8 kg/m<sup>3</sup>, and water in the underlying Gachsaran Formation had an average TDS of 101.5 kg/m<sup>3</sup> [Van Dam et al., 2009]. These concentrations correspond to fluid densities of 1180 and 1075 kg/m<sup>3</sup>, respectively (at 20°C). Samples of ponded surface water in the study area after a rain event ranged in density from 1213 to 1371 kg/m<sup>3</sup> [Wood et al., 2002], with an average density of 1280 kg/m<sup>3</sup> within 10 km of our study site [Van Dam et al., 2009]. The high concentration and density of the surface water are due to dissolution of the sodium, calcium, magnesium, chloride, and nitrate evaporite crust [Wood et al., 2002].

Water and solute budgets for the sabkha by Wood et al. [2002] document that the vast majority of the solutes in the sabkha aquifer have likely come from ascending geologic brines from the underlying formation. The bulk of the water flux in and out is from local rainfall and evaporation. Due to the low hydraulic gradient, the solutes have a residence time in the aquifer of ~6000 years, whereas water in the aquifer has a residence time of only ~50 years [Wood et al., 2002]. Chemical analyses of sabkha aquifer samples at the field site and in the broader region show that sodium and chloride are the dominant ions in solution [Wood et al., 2002; Eustice, 2011], making halite the most common salt to precipitate at the surface.

Next, we assessed the quantity of salts that will under average conditions, precipitate at or near the surface. Sodium, the limiting ion in halite precipitation, has a concentration of 92.8 kg/m<sup>3</sup>. Considering a 1 m<sup>2</sup> area and a potential evaporative flux of 50–88 mm/yr, which represent conservative and high estimates, respectively [Sanford and Wood, 2001], the amount of sodium precipitated would be 50 L × 92.8 kg/m<sup>3</sup> = 4.64 kg Na (8.17 kg Na using 88 L of water). The equivalent mass of Cl that would be precipitated ranges between 7.16 and 12.6 kg for the same range of evaporative flux. Dividing the sum of Na and Cl mass by the density of NaCl (2160 kg/m<sup>3</sup>) leads to a deposition rate of 5.5 × 10<sup>-3</sup> to 9.6 × 10<sup>-3</sup> m<sup>3</sup> of halite per year over the 1 m<sup>2</sup> area. This is equivalent to a deposition rate of 5.5–9.6 mm/yr. We used the Pitzer equation in PHREEQC to estimate that 32–57 mm/yr of precipitation is necessary to dissolve the halite at the same rate as it is being deposited, given the estimated deposition rates, the solubility of halite, and the average shallow water temperature of 30°C. Based on the average rainfall of 32 mm/yr (Figure 2) there should be a surplus of dissolvable halite in the system of up to 4.5 mm/yr at the highest evaporative flux. Considering the period of below-average rainfall prior to 2008, this surplus is a conservative estimate.

**3. Conceptual Models**

To initiate fluid instability in a groundwater system, the density contrast must increase at rates that outpace rates at which diffusion and advection reduce the concentration gradients. In the UAE sabkha aquifer, two conceptual models may reasonably explain the formation of a density inversion that drives convection in this system:

1. Rainfall-induced dissolution of the halite-dominated crust and subsequent infiltration lead to accumulation of the dense brine at the top of the water table. In this model, the density contrast builds up rapidly.

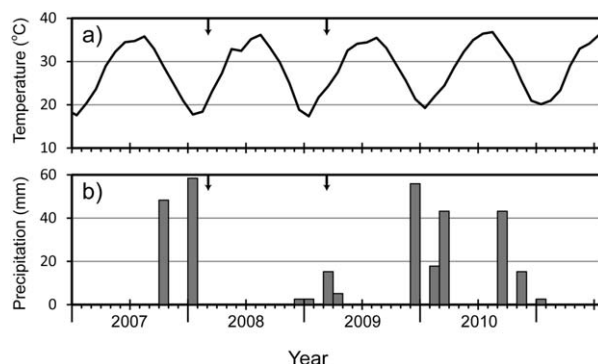


**Figure 3.** Graphs of (a) monthly average air temperature and (b) monthly rainfall from 2007 to mid-2011. ER data collection periods are indicated using arrows.

2. Slow upwelling of low-density water from the Miocene formation below the aquifer is another mechanism to create a density inversion, but at the base of the aquifer.

Evapoconcentration is also often given as a possible mechanism for unstable fingering to develop in these systems [e.g., *Nield et al., 2008*]. However, recent work suggests that evaporation may lead to some water vapor to diffuse downward, causing dilution [*Gran et al., 2011*].

Owing to the large rainfall event immediately preceding the 2008 data collection (Figure 3), which was larger than the average annual rainfall, *Van Dam et al.*

[2009] postulated that this rainfall event was the most likely cause for the observed fingering. In this paper we make the first conceptual model of our hypothesis and then test this using new time-lapse geophysical measurements along with new flow and transport simulations of the system. The alternative conceptual model of upwelling low-density water was also modeled, as described in section 6.

#### 4. Geophysical Measurements

##### 4.1. Background

The ER imaging method uses numerous electrode combinations along an array to generate tomographic images of apparent resistivity in the subsurface [*Dahlin and Zhou, 2004; Jayawickreme et al., 2010*]. ER imaging has successfully been used to characterize the distribution of saline and fresh waters in coastal [*Kruse et al., 1998; Nowroozi et al., 1999; Tronicke et al., 1999; Slater and Sandberg, 2000*] and inland settings [*Acworth, 1999; Acworth and Dasey, 2003; Ong et al., 2010*], subsurface heterogeneity and anisotropy [e.g., *Samouëlian et al., 2003; Greve et al., 2010*], and saline fluid migration [e.g., *Ward et al., 2010*]. The depth of investigation, resolution, and sensitivity of different array types is related to electrode separation and configuration [e.g., *Szalai and Szarka, 2008*]. Petrophysical transform functions, which can be developed in the laboratory, are necessary to interpret the resistivity data in terms of the hydrological properties of interest.

Analysis of ER data requires inversion of apparent resistivities, which is typically achieved through an iterative process [e.g., *Pelton et al., 1978; Loke and Barker, 1996*]. Smoothness constraints are commonly used to choose between multiple models that fit the data and ensure that the resulting model explains the observed values to an acceptable level, while avoiding large spikes in the modeled resistivity values. Potential drawbacks of this procedure included the fact that errors in the data and uncertainties about resolution and uniqueness of the inverted field directly translate to the hydrologic analysis [*Ramirez et al., 2005; Hinnell et al., 2010*] and related challenges to completely recover the solute mass from resistivity data [e.g., *Singha et al., 2008; Pollock and Cirpka, 2010*]. Nevertheless, many examples show excellent correlations between measured resistivity distributions and subsurface fluid properties [e.g., *Amidu and Dunbar, 2008; Hermans et al., 2012*].

##### 4.2. Implementation

In this study, three 2-D surface arrays with 84 electrodes each were used. Two of these arrays (A and B) had 1 m electrode spacing and were laid out in perpendicular directions (Figure 4). A third array (C), parallel to array B, had 0.5 m electrode spacing. To eliminate errors due to positioning differences in subsequent data collection periods, the three transects used permanently installed graphite electrodes. During field campaigns, the electrodes of 0.15 m length and 0.01 m diameter were connected to a switchbox (multiplexer) and eight-channel resistivity meter from Advanced Geosciences Inc. (AGI) using a lightweight multicore cable constructed from Cat5e wire (Figure 4).

The electrical resistivity data were collected using dipole-dipole and pole-pole arrays using identical instrument and measurement settings in subsequent years in 2008 and 2009 (Figure 3). The pole-pole data,

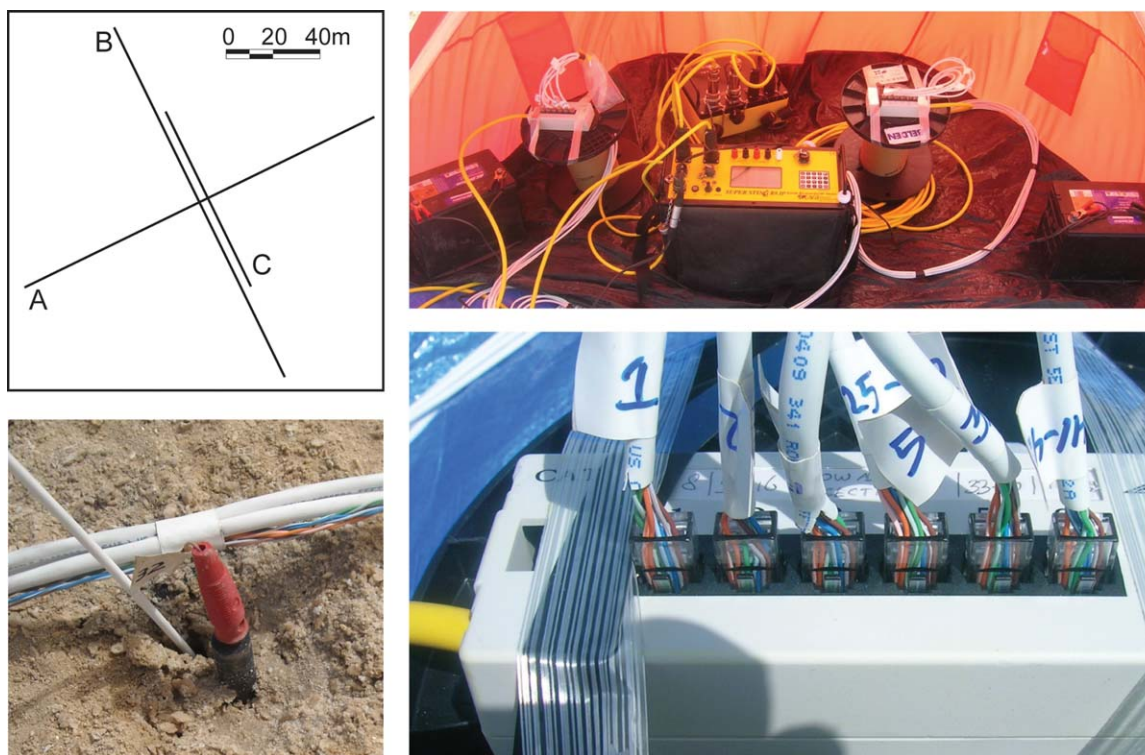


**Figure 4.** Details of field setup. Counterclockwise from top left: Layout of geophysical survey lines (see Figure 1 for location), an installed graphite electrode connected to a custom multicore cable (Cat5e) via a banana plug, RJ45 plugs to connect Cat5e cables with AGI switchbox, and field setup of electrical resistivity measurement equipment.

which are relatively insensitive to lateral variability in resistivity [Dahlin and Zhou, 2004], were used to establish a 1-D model of the resistivity distribution, which allowed for comparison with the hydrostratigraphic model of the field site. Data collected using the dipole-dipole array type, which is most sensitive to lateral variations in electrical resistivity, were used to obtain 2-D models of the resistivity distribution.

### 4.3. Pole-Pole Sounding Results

A 1-D vertical electrical sounding data set was derived from the multielectrode pole-pole data collected along Line A by averaging the apparent resistivity readings for five adjacent midpoints surrounding the intersection with Line B (Figure 4). The pole-pole array type with two infinity electrodes has relatively low sensitivity to lateral variations but provides the deepest imaging and most stable signal (low error) compared to other arrays. The vertical electrical sounding data were inverted using IPI2win software [e.g., Soupios et al., 2007] to generate a best fit resistivity model. The algorithm uses a linear filtering approach for the forward calculation and a regularized optimization based on Tikhonov's approach to obtain an inverse solution.

Results of the inversion of the 2008 data are given in Table 1. The best fit three-layer model results in a very small root-mean-square error of 0.41%. A 0.7 m thick near-surface layer with resistivity of  $0.72 \Omega\text{m}$  represents the capillary zone with authigenic minerals. The second layer, which represents the sabkha aquifer, has a lower resistivity of  $0.2 \Omega\text{m}$  and a thickness of 16.5 m. The Miocene carbonates below the sabkha have a resistivity of  $0.88 \Omega\text{m}$ . When the second layer is fixed to the expected thickness of 10 m (based on interpolation of depth-to-Miocene from well data), the root-mean-square error increases to 1.89%, which is still acceptably low, and resistivities for the second and third layers change to 0.19 and  $0.69 \Omega\text{m}$ , respectively.

To compare the inversion results with the fluid samples collected from wells surrounding the field site, the resistivity values of layers 2 and 3 from the best fit inversion were converted to fluid conductance values and TDS. The capillary zone was not included in this analysis. Fluid conductance ( $\sigma_f$ ) was calculated using the Archie equation:

**Table 1.** Best Fit Inversion Results of 2008 Pole-Pole Sounding Data for Line A, Results of Fluid Salinity Calculations Using Equation (1), and Comparison of Estimated Solute Concentrations With Measured Averages

Layer	Thickness (m)	Bulk Resistivity ( $\Omega\text{m}$ )	Estimated Fluid Specific Conductance ( $\mu\text{S}/\text{m}$ )	Estimated TDS (mg/L)	Measured TDS (mg/L)
1	0.7	0.72			
2	16.5	0.2	213,000	210,000	275,810
3	$\infty$	0.88	126,000	110,000	101,453

$$\sigma_b = \sigma_f \times \theta^m, \tag{1}$$

where  $\sigma_b$  is the bulk conductivity (reciprocal of bulk resistivity values),  $\theta$  is the porosity, and exponent  $m$  is an empirical value known as the cementation factor. Based on typical literature values,  $m$  was set at 1.5 and 2.0 for the aquifer sand and carbonates, respectively [Lesmes and Friedman, 2005]. Porosity was set at 0.38 for the aquifer sand [Wood et al., 2002] and 0.3 for the Miocene carbonates. Samples from wells near the field site display a strong positive correlation between specific conductance and TDS. Using an empirical relationship ( $\text{TDS} = 1.25 \times \sigma_f - 53,000$ ), based on samples with a solute concentration between 65,000 and 250,000 mg/L [Sanford and Wood, 2001], TDS values were estimated for the sabkha aquifer fluids and the Miocene carbonate fluids. The estimated TDS values are reasonably correlated with measured values (Table 1). The 1-D resistivity data thus confirm the general hydrostratigraphic model for the field site.

#### 4.4. Dipole-Dipole ERI Data

The dipole-dipole electrical resistivity imaging (ERI) data were inverted using EarthImager2D software. Inversion settings were optimized using synthetic (forward) models of apparent resistivity based on simplified models of subsurface salinity and bulk resistivity (Table 1). Initial settings and preprocessing steps are listed in Table 2. In the field, repeat measurements were used to identify unstable quadripoles; data with repeat errors larger than 5% were eliminated from the inversion. No reciprocal measurements were conducted. No temperature correction was applied to the data sets because both data collection periods were in the same month of different years (Figure 3).

The inverted dipole-dipole resistivity data from 2008 are shown in Figure 5a. The top 0.75 m shows the highest resistivity with values around 1.0  $\Omega\text{m}$ . This high-resistivity layer is representative of the capillary zone, below which the resistivity sharply drops and vertical structures of alternating resistivity of around 0.1 and 0.3  $\Omega\text{m}$  start to appear. Most of the vertical low-resistivity structures extend to around 6 m depth; however, a few reach close to the bottom of the profile. The shallow low-resistivity structures have a wavelength of 6.5–7 m, while the deeper structures display an irregular pattern with a wavelength between 10 and 15 m where present [Van Dam et al., 2009]. In the perpendicular line B, the vertical structures of alternating resistivity were equally apparent but spaced at less regular intervals.

**Table 2.** Settings for Inversion of Dipole-Dipole ERI Data

Setting	Value/Type
Minimum voltage (mV)	0.02
Minimum $V/I$ ( $\Omega$ )	$2 \times 10^{-05}$
Minimum apparent resistivity ( $\Omega\text{m}$ )	0.01
Maximum apparent resistivity ( $\Omega\text{m}$ )	10,000
Maximum repeat error (%)	5
Inversion method	Smooth model inversion
Forward modeling method	Finite element method
Forward system solver	Cholesky decomposition
Boundary condition type	Dirichlet
Number of cells between two electrodes	8
Layer-thickness increment	1.1
Inverted model/pseudosection depth	1.1
Maximum number of iterations	8
Stop at RMS error (%)	3
Starting model	Pseudosection

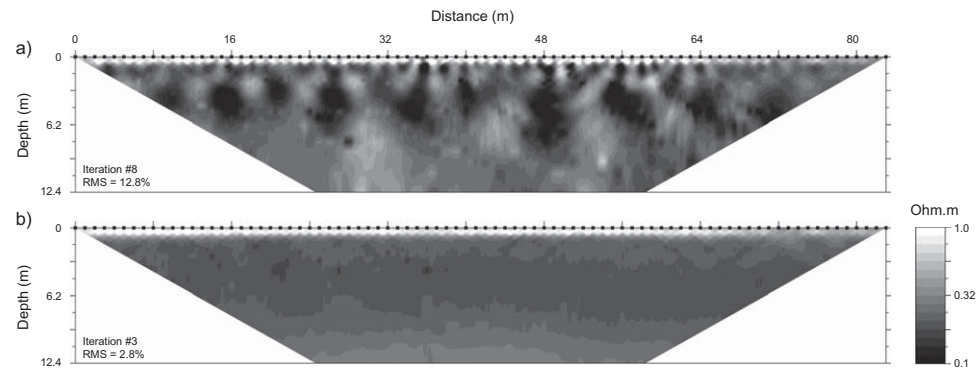


**Figure 5.** Inverted resistivity images from dipole-dipole resistivity surveys for Line A from (a) 2008 and (b) 2009. The log scale shows resistivity ( $\rho$ ). See Figures 1 and 4 for location.

The inverted electrical resistivity profiles from the 2009 field campaign (Figure 5b) are markedly different from the 2008 data (Figure 5a). Most of the resistivity changes occur vertically with minimal lateral variation. Similar to the 2008 data, the capillary zone above the water table has the highest resistivity. When laterally averaged over the middle 40 m of the array, 1-D resistivity profiles from 2008 and 2009 are nearly identical, suggesting that the average vertical salinity distribution has remained fairly constant.

Various steps were undertaken to test the stability of the inversion results from 2008 and 2009. We checked for possible negative impact of “bad electrodes” on inversion errors by synthetic modeling and found the possible effects to be minimal for the chosen settings [Eustice, 2011]. Synthetic modeling for a simple two-layer system (representing an unsaturated zone over a low-resistivity layer of infinite depth) indicated that the rhythmic near-surface variations in the very shallow high-resistivity zone of both Figures 5a and 5b are an artifact, caused by the presence of a sharp resistivity boundary at the water table. A mesh size was chosen to avoid instability and provide reproducible results in the inversions.

The significant lateral variations in resistivity for the 2008 ERI data set are consistent with unstable fingering (Figure 5a). The vertical low-resistivity features appear to be high-density fingers that are descending through the aquifer, while the high-resistivity features are ascending lighter fluids. There are no obvious vertical features and very little lateral variation in resistivity in the 2009 data, suggesting that convective fingering is absent (Figure 5b). Analysis of the geophysical data thus suggests that free convection is episodic. Through numerical modeling we will address the previously discussed hypothesis that the process driving free convection in this system is rainfall-induced dissolution of the halite crust. Alternative models of upwelling of low-density water and evapoconcentration of sabkha water are addressed in section 6.

## 5. Numerical Modeling

### 5.1. Background

In simple free convective systems, the onset of instability has traditionally been assessed using the nondimensional Rayleigh number ( $Ra$ ), which is the ratio between buoyancy-driven forces and resistive forces caused by diffusion and dispersion:

$$Ra = \frac{U_c H}{D_0} = \frac{g \kappa \Delta \rho H}{\theta \mu D_0}, \quad (2)$$

where  $U_c$  is the convective velocity,  $H$  is the thickness of the porous layer,  $D_0$  is the molecular diffusion coefficient,  $g$  is the magnitude of gravitational acceleration ( $m/s^2$ ),  $\kappa$  is the intrinsic permeability,  $\Delta \rho$  is the difference between maximum and minimum densities,  $\theta$  is the porosity, and  $\mu$  is the dynamic viscosity of the fluid ( $kg/m \cdot s$ ). For the classical problem of infinite conducting plates the instability criterion is defined as  $Ra_c = 4\pi^2$ . In the sabkha system, the exact  $Ra_c$  is unknown, but smaller than the common maximum of  $4\pi^2$  [Nield and Bejan, 2006]; assumptions include steady-state flow and independence of mechanical dispersion and convective flow velocity. Also, the approach requires averaging of spatially variable properties and time-dependent length scales [Simmons, 2005]. Some researchers have argued that during early times,

the medium must be considered of semi-infinite thickness, rendering equation (2) irrelevant for initial finger development [e.g., *Hidalgo and Carrera, 2009*]. Nevertheless, it is worth noting that  $Ra$  for the sabkha system (calculated by *Van Dam et al. [2009]* as  $2.7 \times 10^4$ ) is orders of magnitude larger than the commonly used values for  $Ra_c$ , including that associated with the classical Rayleigh-Benard convection [*Nield and Bejan, 2006, Table 6.1*]. Convection is thus expected to occur.

In recent years, significant advances have been made in continuum modeling of convective processes in porous media [e.g., *Zoia et al., 2009; Post and Simmons, 2010; Xie et al., 2011*]. To simulate the time evolution of the convective process in the UAE aquifer, we performed a hydrodynamic simulation using COMSOL Multiphysics software solving fluid and solute mass balance equations. We tested the software using the classic Elder problem as a benchmark and found that it functioned as expected.

Fluid flow is calculated by Darcy's law:

$$u = -\frac{\kappa}{\mu}(\nabla p + \rho g \nabla z), \tag{3}$$

where  $u$  is the Darcy velocity or specific discharge vector (m/s),  $\kappa$  ( $m^2$ ) is the permeability,  $p$  is the fluid pressure (Pa), and  $\nabla z$  is a unit vector in the direction over which the gravity acts (m).

Darcy's law is then inserted into a continuity equation:

$$\frac{\partial}{\partial t}(\rho\theta) + \nabla(\rho u) = 0, \tag{4}$$

to obtain

$$\frac{\partial}{\partial t}(\rho\theta) + \nabla \rho \left[ -\frac{\kappa}{\mu}(\nabla p + \rho g \nabla z) \right] = 0. \tag{5}$$

Since solute transport is taking place in a fully saturated medium and we assume that the solutes are conservative, transport can be modeled using a simplified advection-dispersion equation without adsorption and desorption terms:

$$\theta_s \frac{\partial C}{\partial t} + \nabla C u - \nabla(\theta_s D \nabla C) = 0, \tag{6}$$

where  $\theta_s$  is the fluid's volume fraction (equal to porosity in saturated medium),  $C$  is the fluid concentration, and  $D$  is the hydrodynamic dispersion tensor [e.g., *Bear, 1972*]. We chose a dispersivity of 8 cm based on literature analysis and sensitivity analysis runs, providing results that were in qualitative agreement with the resistivity inversion.

### 5.2. Implementation

The sabkha system was modeled in 2-D using a 30 m × 10.13 m (width × height) model domain. Vertically, the domain is divided into two horizontal layers: the 10 m thick bottom layer represents the aquifer in

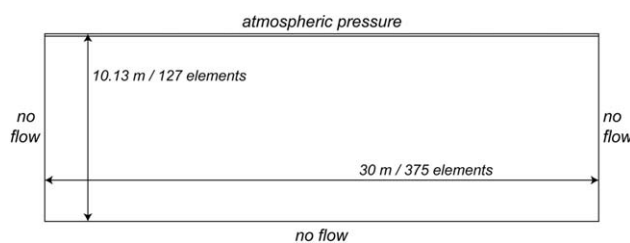


**Figure 6.** Geometry and boundary conditions for the simulation. Parameter values are listed in Table 3.

absence of infiltrating rainwater, whereas the top layer represents the increased saturated thickness due to recharge (Figure 6). The thickness of the upper layer is a function of the amount of rainfall (0.05 m) divided by the porosity (0.38), with the fluid solute concentration in this layer depending on the mass of halite available in the surface crust. This model design assumes that at the start of the

**Table 3.** Model Parameters, Values, and Sources Used in COMSOL Modeling

Parameter	Value	Unit	Source
Domain height ( $L$ )	10	m	Van Dam et al. [2009]
Density of aquifer water ( $\rho_0$ )	1180	kg/m <sup>3</sup>	Wood et al. [2002]
Density of infiltrating water ( $\rho_s$ )	1305	kg/m <sup>3</sup>	Wood et al. [2002]
Concentration of aquifer water ( $C_0$ )	275.8	kg/m <sup>3</sup>	Wood et al. [2002]
Concentration of infiltrating water ( $C_s$ )	440	kg/m <sup>3</sup>	Wood et al. [2002]
Dynamic viscosity ( $\mu$ )	0.001	kg/m s	Assumed for fresh water
Hydraulic conductivity ( $K$ )	6.57	m/d	Measured
Porosity ( $\theta$ )	0.38		Wood et al. [2002]
Dispersivity ( $\alpha$ ) (lateral and transverse)	0.08	m	Schulze-Makuch [2005]
Pressure ( $p$ )	1	atm	Assumed for sea level
Acceleration of gravity ( $g$ )	9.81	m/s <sup>2</sup>	Constant

simulation, rainfall has infiltrated through the capillary zone to the top of the water table to extend the saturated thickness of the aquifer.

The model domain was discretized using a structured quadrilateral mesh with cell sizes between 0.065 m × 0.08 m for the top layer and 0.08 m × 0.08 m for the bottom layer. The maximum cell size in the mesh was determined by the critical Peclet number to avoid numerical instability of the model. All four boundaries of the model are considered no solute flux, with no mass flowing in or out, and a total flux equal to zero:  $n \cdot (Cu - D \cdot \nabla C) = 0$ , where  $n$  is a vector normal to the boundary. Similarly, the same edges of the model domain are treated as no-flow boundaries:  $n/\mu(\nabla p + \rho g \nabla z) = 0$ . The assumption of lateral no-flow and no-flux boundaries is reasonable because the horizontal hydraulic advection rate at our site is too small to significantly affect convective fingering. Additionally, the influence on the system of the upwelling from the formation below the aquifer is orders of magnitude smaller than that of a large rainfall event so that vertical flux and flow out of the bottom boundary of the system can be ignored. The top boundary is treated as an atmospheric pressure boundary with a pressure of  $p_0 = p_{ATM}$  and a zero solute flux. The inflow due to recharge was simulated by emplacing a 13 cm thick zone of fluid with the concentration of the measured ponded water on top of the fresher aquifer water (Figure 6). For the temporal discretization we used a setting that allowed for a varying time step dependent to maintain stability of the solution.

To represent the conditions and processes of the system as accurately as possible, input parameters characteristic of and mostly identical to the field conditions were used. These were obtained by field measurements or from the relevant literature (Table 3). The starting model simulated the first of two rainfall events that preceded the 2008 ERI data collection. Based on the calculated infiltration time of approximately 5 weeks we assume that the second event would have had a limited impact on the initial formation of fingers.

### 5.3. Results

The simulation period was 52 weeks. During the first few weeks of the simulation, many small high-concentration fingers quickly developed from the top layer and began descending into the bottom layer of the model (Figure 7). The location of these fingers appeared to not be tied to the mesh discretization, as the same number of fingers developed independent of mesh characteristics. Initially, the model developed small fingers with a wavelength of around 0.8 m. Over time, the small fingers began to coalesce into fewer and larger fingers, as expected [e.g., Elder, 1967; Kolditz et al., 1998], with wavelengths of up to around 1.5 and 3 m for the middle and lower parts of the model domain, respectively. Multiple realizations produced similar results. Small numerical instabilities would occasionally develop during the simulations, but these did not impact model results.

A quantitative estimate of the convective velocity of high-density fingers is needed to assess whether the fingers are expected to be present during any of the three ERI data collection campaigns. We calculated the velocity of the infiltrating solute mass using the deepest point of the infiltration front (DPF) approach [e.g., Xie et al., 2011]. DPF is the deepest point in the model domain of the interface between the dense plume and the background fluid. We defined the DPF interface as the concentration with  $C = 0.01 \times (C_s - C_0)$ . DPF velocity gives a maximum estimate of the finger descent rate and is closest to the theoretical

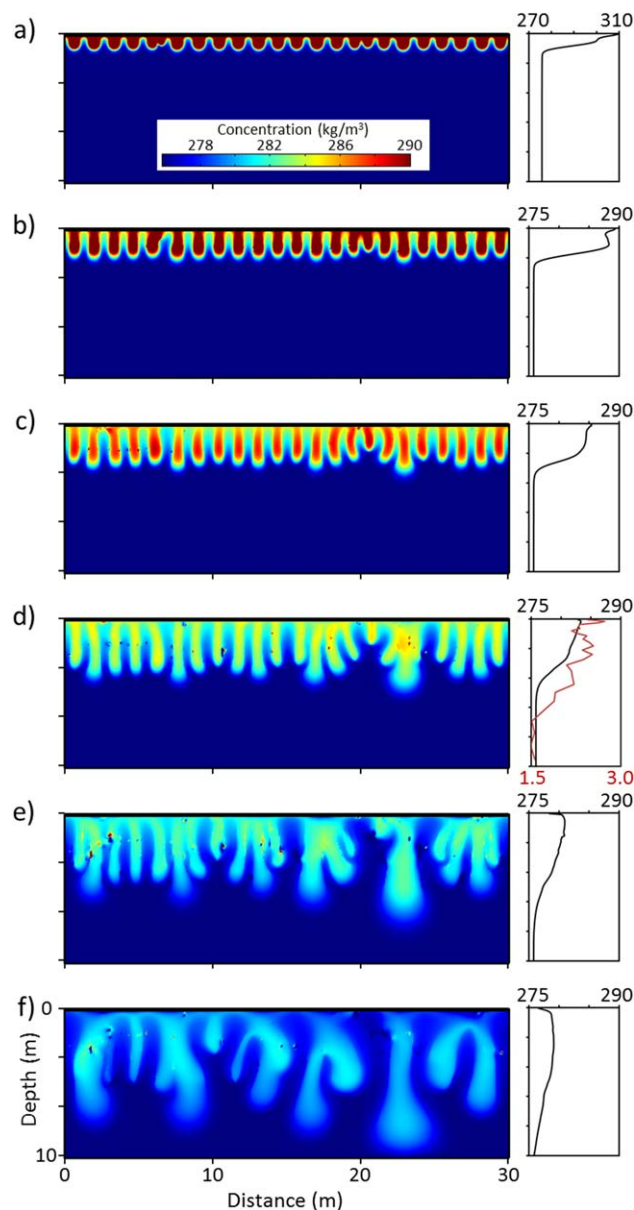


**Figure 7.** Fluid concentrations after (a) 1, (b) 3, (c) 7, (d) 15, (e) 29, and (f) 52 weeks from the start of simulation. The model domain is 30 m wide by 10.13 m high (Figure 6). The starting concentration of the infiltrating water is 440 kg/m<sup>3</sup>, and background fluid has a concentration of 275.6 kg/m<sup>3</sup>. Other modeling parameters are given in Table 3. The graphs on the right show 1-D concentration depth profiles (laterally integrated fluid concentrations) for the model domain; note the different concentration scale for Figure 7a. The 1-D plot at (d) includes a comparison with the laterally integrated (1-D) bulk conductivity, obtained from Figure 5a, in red.

the simulation, high-density fingers had descended into the lower-density fluid to approximately 4 m depth (Figure 7d). The geophysical imaging shows a similar pattern with fingers descending approximately 6 m into the aquifer. The observed differences can be the result of the limited resolution of ER data with increasing depth as well as differences in hydraulic properties and densities between the model and the natural system. Also, the process was modeled in 2-D, whereas the real convection progresses in 3-D.

The 2-D geophysical images were laterally integrated, similar to the concentration depth profiles in Figure 7. The 1-D bulk electrical conductivity obtained by this lateral averaging was plotted in Figure 7d. The

speed of  $U_c = (K/\theta) \times (\Delta\rho/\rho_0)$  [Xie *et al.*, 2011]. An alternative approach to estimate fingering speed is via calculation of the center of mass (COM), which is typically significantly slower than DPF velocity. COM velocity is based on the calculation of solute concentrations that have been laterally integrated for the model domain [e.g., Post and Kooi, 2003]. Since our model uses a finite solute source, the resulting laterally averaged concentration profiles become very smooth (Figure 7), which limits the usefulness of the COM velocity.

Although recent work demonstrates that calculation of the convective velocity is considerably more complicated than previously thought [Xie *et al.*, 2012], our calculated velocities provide a useful first-order estimate. The DPF rate of finger descent was initially relatively fast, with speeds of around 0.2 m/d in the first week (Figure 8). The rate of descent slowed over time to around 0.02 m/d near the end of the 1 year simulation period. The finger descent slows due to factors including fluid entrainment, mechanical dispersion and molecular diffusion that reduce the density within fingers, and upwelling of lower-density fluid between neighboring fingers [Xie *et al.*, 2011]. In later times, the physical limitations of the model domain may also play a role in the velocity reduction.

## 6. Discussion

### 6.1. Comparing Modeling and ER Results

Key characteristics of the COMSOL simulation results are similar to the geophysical inversion models (spatial patterns, temporal evolution of the complex fingering, and solute concentrations), although there are also differences. At  $t = 15$  weeks from the start of

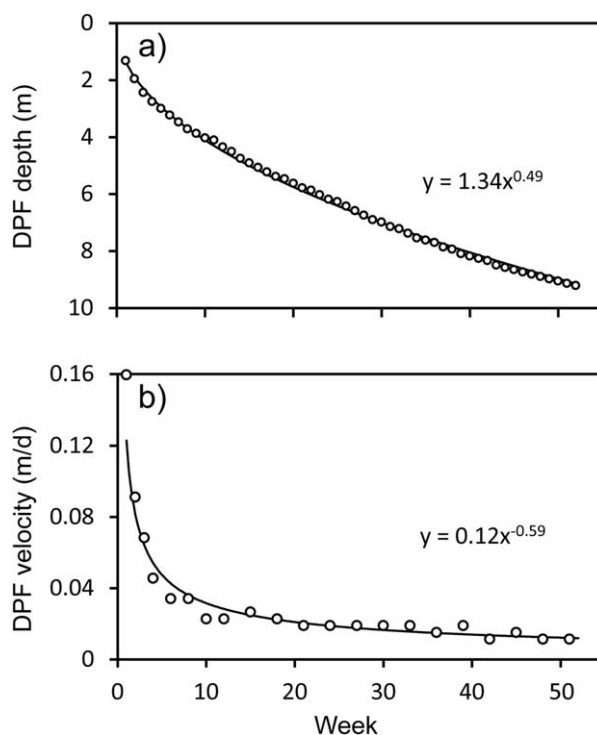


**Figure 8.** Graphs of (a) the deepest point of the infiltration front (DPF) for the 52 week simulation and (b) derived DPF velocity in meters per day.

pattern of a decrease in electrical conductivity with depth is similar to the changes in fluid salinity from the COMSOL simulations. The bulk conductivity data were converted to concentration and fluid salinity using the Archie equation and parameters discussed previously ( $\rho = 0.76C + 972.45$ , based on data in Sanford and Wood [2001]). The 1-D TDS profile obtained from the geophysical data is comparable to the TDS distribution from the transport model. The DPF value obtained from the geophysical data is 1–2 m larger than that calculated based on the transport model. However, as discussed earlier, a direct match is not expected. This is due to differences in modeling and measurement approaches but also because instabilities are semichaotic by nature that cannot be expected to match exactly.

The joint results of the experimental ER imaging and the numerical simulations suggest that some important questions about this process in natural

systems [Simmons, 2005] may start to be answered. This work provides information on the scalability of experimental results and numerical simulations. Our work also suggests that future investigations will be able to address the relative importance of various modeling simplifications that are made in models of unstable fingering. Finally, our work suggests that geophysics is a powerful alternative method to characterize these systems, although it may never be possible to completely replace direct head measurements or other field data.

### 6.2. Rainfall-Induced Dissolution of Halite

Concentration differences between the ponded surface water and the sabkha aquifer were found to be as high as  $250 \text{ kg/m}^3$  [Wood et al., 2002]. The Rayleigh number for this concentration difference is orders of magnitude higher than the common instability criterion ( $4\pi^2$ ). Two major rainfall events of 50 and 64 mm took place 18 and 6 weeks, respectively, before the first data collection period in March 2008 (Figure 3). Based on the amount of halite in the surface crust and capillary zone, both events had the potential to become completely saturated with dissolved halite. Considering the timing of these rainfall events it is likely that a dense brine infiltrated to the water table prior to the field visit in 2008 (Figure 3). By taking into account the  $\sim 25$  days for infiltration through the capillary zone [Eustice, 2011] we assume that the fingers would have had around 15 weeks to develop. The second rainfall event, 6 weeks before the field visit in 2008, would have had limited impact on convective fingering, as only 2–3 weeks would have been available for a second set of fingers to develop. This event may, however, have further increased the TDS near the water table. For both events, overland flow may have affected the total influx; however, based on falling-head infiltrometer experiments [Eustice, 2011] and the low gradient of the site [Wood et al., 2012], overland flow would have been minimal.

Total rainfall in the year prior to the 2009 field campaign was very small with a total of 18 mm of rain during the 2008–2009 water year. Although the transport simulation results suggest that the fingering would have still been present (Figure 7), the contrast in solute concentration between descending fingers and upwelling sabkha water was significantly reduced by diffusion. We therefore believe that the remaining concentration differences would have been below the resolution of the ER measurements.

### 6.3. Alternative Model

Analysis of water samples from the sabkha aquifer and the underlying Miocene formation shows a large density difference [Wood *et al.*, 2002; Van Dam *et al.*, 2009]. The contrast is well above the typical Rayleigh instability criterion, suggesting that the continuous upwelling of lower-density water (driven by the rainfall deficit and small regional hydraulic gradient) may also lead to unstable free convection. Unknown variables in this system are the likely gentle gradient of the density contrast and the possible negative effect of the porosity difference on the development of convective flow.

Using the same model domain and boundary conditions as described earlier, this process was simulated in COMSOL. We used a continuous source at the bottom of the domain with a  $\Delta C$  of  $174.3 \text{ kg/m}^3$  and ran a simulation for 33 years. The results indicate that these conditions do enable free convection to develop. However, the concentration difference of the fingers was an order of magnitude smaller than that associated with the infiltration of rainfall-induced brine, and thus possibly below the resolution of the electrical imaging. Also, the process took multiple years to develop, which suggests that it would not be present in 2009 after the homogenizing effect of the rainfall-induced fingering episode in 2008.

## 7. Conclusions

Results from time-lapse geophysical characterization and hydrodynamic modeling of transient free convection in a shallow homogeneous-sand sabkha aquifer in the United Arab Emirates are presented. This is the first quantitative, systematic evaluation of free convection dynamics in the field using a combination of direct field evidence and modeling. Electrical resistivity data collected in 2008 and 2009 demonstrated that free convection in this system is not at steady state. A complex fingering pattern that was observed in 2008 data was not present in later data sets.

Based on the hypothesis that the convective fingering in 2008 was enabled by the downward infiltration of a dense brine after the rainfall-induced dissolution of the halite crust of the sabkha, we developed a halite budget that indeed suggests a very dense brine likely formed. 2-D numerical modeling of a density inversion was performed using this halite budget, measured fluid densities, and the observed rainfall event. The results of this simulation demonstrate that free convection in this system is possible, and that the timing for the development of fingers in the model coincides with the timing of electrical resistivity data collection in 2008. Moreover, the vertical distribution of fluid concentrations for the model domain (laterally integrated) is consistent with the estimated fluid concentrations from the inverted electrical resistivity data. The rapid decay rate of the fingering in the numerical model also explains the lack of complex fingering in the subsequent data collection period. In support of previous field and numerical work, this study highlights the importance of the transient character of free convection phenomena in natural systems. It has important implications not only for sabkhas, but also for other places around the world (e.g., salt lakes) where episodic convection is expected to take place.

Critically, this paper provides important direct field measurements in a discipline (variable density groundwater flow) where field data and especially direct observational evidence are quite rare. There are only a few papers that provide direct evidence of fingering in the field. This paper is the first to provide such direct and independent evidence, coupled with time series data, to allow for quantifying the speed and the dynamics of free convective fingering in a field setting. This is a major step forward for the study of free convection. Temporal data sets such as the one presented here are critical to improve our understanding of the dynamics of free convection in field systems. More generally, studies such as the one presented here are critical to complement, reconcile, test, validate, and indeed balance the huge number of theoretical and modeling studies on this topic that exist in the literature.

### Acknowledgments

This work was supported by grants from NSF (EAR-0903508 and EAR-0930022); any opinions, findings, and conclusions or recommendations expressed are those of the authors and do not necessarily reflect the views of the NSF. We acknowledge Don Nield of the University of Auckland for insightful discussions, Wade Kress and Dave Clark of USGS/NDC for logistical assistance, and Steve Hamilton of MSU KBS for fluid chemistry measurements. We thank three anonymous reviewers for their constructive comments on this paper.

## References

- Acworth, R. I. (1999), Investigation of dryland salinity using the electrical image method, *Aust. J. Soil Res.*, 37(4), 623–636.
- Acworth, R. I., and G. R. Dasey (2003), Mapping of the hyporheic zone around a tidal creek using a combination of borehole logging, borehole electrical tomography and cross-creek electrical imaging, New South Wales, Australia, *Hydrogeol. J.*, 11, 368–377.
- Amidu, S. A., and J. A. Dunbar (2008), An evaluation of the electrical-resistivity method for water-reservoir salinity studies, *Geophysics*, 73(4), G39–G49.
- Bauer, P., R. Supper, S. Zimmermann, and W. Kinzelbach (2006), Geoelectrical imaging of groundwater salinization in the Okavango Delta, Botswana, *J. Appl. Geophys.*, 60, 126–141.

- Bear, J. (1972), *Dynamics of Fluids in Porous Media*, 764 pp., Elsevier, New York.
- Bottomley, N. (1996), Recent climate in Abu Dhabi, in *Desert Ecology of Abu Dhabi: A Review of Recent Studies*, edited by P. E. Osborne, pp. 36–49, Pisces Publ., Newbury, U. K.
- Cardenas, M. B., A. M. F. Lagmay, B. J. Andrews, R. S. Rodolfo, H. B. Cabria, P. B. Zamora, and M. R. Lapus (2012), Terrestrial smokers: Thermal springs due to hydrothermal convection of groundwater connected to surface water, *Geophys. Res. Lett.*, *39*, L02403, doi:10.1029/2011GL050475.
- Coumou, D., T. Driesner, and C. A. Heinrich (2008), The structure and dynamics of mid-ocean ridge hydrothermal systems, *Science*, *321*(5897), 1825–1828.
- Dahlin, T., and B. Zhou (2004), A numerical comparison of 2D resistivity imaging with 10 electrode arrays, *Geophys. Prospect.*, *52*, 379–398.
- Diersch, H.-J. G., and O. Kolditz (2002), Variable-density flow and transport in porous media: Approaches and challenges, *Adv. Water Resour.*, *25*, 899–944.
- Elder, J. W. (1967), Steady free convection in a porous medium heated from below, *J. Fluid Mech.*, *27*(1), 29–48.
- Eustice, B. P. (2011), Exploring the nature of free convection in a sabkha with electrical imaging and hydrological modeling, MSc thesis, Dep. of Geol. Sci., Mich. State Univ., East Lansing, Mich.
- Fan, Y., C. J. Duffy, and D. S. Oliver Jr. (1997), Density-driven groundwater flow in closed desert basins: Field investigations and numerical experiments, *J. Hydrol.*, *196*, 139–184.
- Garven, G., M. S. Appold, V. I. Toptygina, and T. J. Hazlett (1999), Hydrogeologic modeling of the genesis of carbonate-hosted lead-zinc ores, *Hydrogeol. J.*, *7*(1), 108–126.
- Gran, M., J. Carrera, S. Olivella, and M. W. Saaltink (2011), Modeling evaporation processes in a saline soil from saturation to oven dry conditions, *Hydrol. Earth Syst. Sci.*, *15*, 2077–2089.
- Greve, A. K., R. I. Acworth, and B. F. J. Kelly (2010), Detection of subsurface soil cracks by vertical anisotropy profiles of apparent electrical resistivity, *Geophysics*, *75*(4), WA85–WA93.
- Hermans, T., A. Vandenbohede, L. Lebbe, R. Martin, A. Kemna, J. Beaujean, and F. Nguyen (2012), Imaging artificial salt water infiltration using electrical resistivity tomography constrained by geostatistical data, *J. Hydrol.*, *438*, 168–180.
- Hidalgo, J. J., and J. Carrera (2009), Effect of dispersion on the onset of convection during CO<sub>2</sub> sequestration, *J. Fluid Mech.*, *640*, 441–452.
- Hinnell, A. C., T. P. A. Ferré, J. A. Vrugt, J. A. Huisman, S. Moysey, J. Rings, and M. B. Kowalsky (2010), Improved extraction of hydrologic information from geophysical data through coupled hydrogeophysical inversion, *Water Resour. Res.*, *46*, W00D40, doi:10.1029/2008WR007060.
- Hodgkinson, J., M. E. Cox, and S. McLoughlin (2007), Groundwater mixing in a sand-island freshwater lens: Density-dependent flow and stratigraphic controls, *Aust. J. Earth Sci.*, *54*, 927–946.
- Jayawickreme, D. H., R. L. Van Dam, and D. W. Hyndman (2010), Hydrological consequences of land-cover change: Quantifying the influence of plants on soil moisture with time-lapse electrical resistivity, *Geophysics*, *75*(4), WA43–WA50, doi:10.1190/1.3464760.
- Koch, M., and G. Zhang (1992), Numerical solution of the effects of variable density in a contaminant plume, *Ground Water*, *30*(5), 731–742.
- Kolditz, O., R. Ratke, H. J. G. Diersch, and W. Zielke (1998) Coupled groundwater flow and transport: 1. Verification of variable density flow and transport models, *Adv. Groundwater Resour.*, *21*(1), 27–46.
- Kooi, H., J. Groen, and A. Leijnse (2000), Modes of seawater intrusion during transgressions, *Water Resour. Res.*, *36*(12), 3581–3589, doi:10.1029/2000WR900243.
- Kruse, S. E., M. R. Brudzinski, and T. L. Geib (1998), Use of electrical and electromagnetic techniques to map seawater intrusion near the Cross-Florida Barge Canal, *Environ. Eng. Geosci.*, *4*(3), 331–340.
- Lesmes, D. P., and S. P. Friedman (2005), Relationships between the electrical and hydrogeological properties of rocks and soils, in *Hydrogeophysics*, edited by Y. Rubin and S. S. Hubbard, pp. 87–128, Springer, Dordrecht, Netherlands.
- Liu, H. H., and J. H. Dane, (1996), A criterion for gravitational instability in miscible dense plumes, *J. Contam. Hydrol.*, *23*, 233–243.
- Loke, M. H., and R. D. Barker (1996), Rapid least-squares inversion of apparent resistivity pseudosections using a quasi-Newton method, *Geophys. Prospect.*, *44*, 131–152.
- Nield, D. A., and A. Bejan (2006), *Convection in Porous Media*, Springer, New York.
- Nield, D. A., C. T. Simmons, A. V. Kuznetsov, and J. D. Ward (2008), On the evolution of salt lakes: Episodic convection beneath an evaporating salt lake, *Water Resour. Res.*, *44*, W02439, doi:10.1029/2007WR006161.
- Nowroozi, A. A., S. B. Horrocks, and P. Henderson (1999), Saltwater intrusion into the freshwater aquifer in the eastern shore of Virginia: A reconnaissance electrical resistivity survey, *J. Appl. Geophys.*, *42*(1), 1–22.
- Ong, J. B., J. W. Lane, V. A. Zlotnik, T. Halihan, and E. A. White (2010), Combined use of frequency-domain electromagnetic and electrical resistivity surveys to delineate near-lake groundwater flow in the semi-arid Nebraska Sand Hills, USA, *Hydrogeol. J.*, *18*, 1539–1545.
- Pelton, W. H., L. Rijo, and C. M. Swift Jr. (1978), Inversion of two-dimensional resistivity and induced-polarization data, *Geophysics*, *43*, 788–803.
- Pollock, D., and O. A. Cirpka (2010), Fully coupled hydrogeophysical inversion of synthetic salt tracer experiments, *Water Resour. Res.*, *46*, W07501, doi:10.1029/2009WR008575.
- Post, V. E. A., and H. Kooi (2003), Rates of salinization by free convection in high-permeability sediments: Insights from numerical modeling and application to the Dutch coastal area, *Hydrogeol. J.*, *11*(5), 549–559.
- Post, V. E. A., and C. T. Simmons (2010), Free convective controls on sequestration of salts into low-permeability strata: Insights from sand tank laboratory experiments and numerical modeling, *Hydrogeol. J.*, *18*(1), 39–54.
- Ramirez, A. L., J. J. Nitao, W. G. Hanley, R. Aines, R. E. Glaser, S. K. Sengupta, K. M. Dyer, T. L. Hickling, and W. D. Daily (2005), Stochastic inversion of electrical resistivity changes using a Markov Chain Monte Carlo approach, *J. Geophys. Res.*, *110*, B02101, doi:10.1029/2004JB003449.
- Riaz, A., M. Hesse, H. A. Tchelepi, and F. M. J. Orr (2006), Onset of convection in a gravitationally unstable diffusive boundary layer in porous media, *J. Fluid Mech.*, *548*, 87–111.
- Samouëlian, A., I. Cousin, G. Richard, A. Tabbagh, and A. Bruand (2003), Electrical resistivity imaging for detecting soil cracking at the centimetric scale, *Soil Sci. Soc. J. Am.*, *67*, 1319–1326.
- Sanford, W. E., and W. W. Wood (2001), Hydrology of the coastal sabkhas of Abu Dhabi, United Arab Emirates, *Hydrogeol. J.*, *9*(4), 358–366.
- Schincariol, R. A., and F. W. Schwartz (1990), An experimental investigation of variable density flow and mixing in homogeneous and heterogeneous media, *Water Resour. Res.*, *26*(10), 2317–2329, doi:10.1029/WR026i010p02317.
- Schulze-Makuch, D. (2005), Longitudinal dispersivity data and implications for scaling behavior, *Ground Water*, *43*(3), 443–456.
- Simmons, C. T. (2005), Variable density groundwater flow: From current challenges to future possibilities, *Hydrogeol. J.*, *13*, 116–119.

- Simmons, C. T., T. R. Fenstemaker, and J. M. Sharp Jr. (2001), Variable density groundwater flow and solute transport in heterogeneous porous media: Approaches, resolutions and future challenges, *J. Contam. Hydrol.*, *52*(1–4), 245–275.
- Singha, K., A. Pidlisecky, F. D. Day-Lewis, and M. N. Gooseff (2008), Electrical characterization of non-Fickian transport in groundwater and hyporheic systems, *Water Resour. Res.*, *44*, W00D07, doi:10.1029/2008WR007048.
- Slater, L. D., and S. K. Sandberg (2000), Resistivity and induced polarization monitoring of salt transport under natural hydraulic gradients, *Geophysics*, *65*(2), 408–420.
- Soupios, P. M., M. Kouli, F. Vallianatos, A. Vafidis, and G. Stavroulakis (2007), Estimation of aquifer hydraulic parameters from surficial geophysical methods: A case study of Keritis Basin in Chania (Crete – Greece), *J. Hydrol.*, *338*(1–2), 122–131.
- Stevens, J. D., J. M. Sharp Jr., C. T. Simmons, and T. R. Fenstemaker (2009), Evidence of free convection in groundwater: Field-based measurements beneath wind tidal flats, *J. Hydrol.*, *375*, 394–409.
- Szalai, S., and L. Szarka (2008), Parameter sensitivity maps of surface geoelectric arrays: I. Linear Arrays, *Acta Geod. Geophys. Hung.*, *43*(4), 419–437.
- Tronicke, J., N. Blindow, R. Gross, and M. A. Lange (1999), Joint application of surface electrical resistivity- and GPR-measurements for groundwater exploration on the island of Spiekeroog—northern Germany, *J. Hydrol.*, *223*, 44–53.
- Van Dam, R. L., C. T. Simmons, D. W. Hyndman, and W. W. Wood (2009), Natural free convection in porous media: First field documentation in groundwater, *Geophys. Res. Lett.*, *36*, L11403, doi:10.1029/2008GL036906.
- Ward, A. S., M. N. Goosseff, and K. Singa (2010), Imaging hyporheic zone solute transport using electrical resistivity, *Hydrol. Processes*, *24*(7), 948–953.
- Wood, W. W. (2011), An historical odyssey: The origin of solutes in the coastal sabkha of Abu Dhabi, United Arab Emirates, *Int. Assoc. Sedimentol. Spec. Publ.*, *43*, 243–254.
- Wood, W. W., W. E. Sanford, and A. R. S. Al Habschi (2002), The source of solutes in the coastal sabkha of Abu Dhabi, *Bull. Geol. Soc. Am.*, *114*(3), 259–268.
- Wood, W. W., R. M. Bailey, B. A. Hampton, T. F. Kraemer, Z. Lu, D. W. Clark, R. H. R. James, and K. Al Ramadan (2012), Rapid late Pleistocene/Holocene uplift and coastal evolution of the southern Arabian (Persian) Gulf, *Quat. Res.*, *77*(2), 215–220.
- Xie, Y., C. T. Simmons, and A. D. Werner (2011), Speed of free convective fingering in porous media, *Water Resour. Res.*, *47*, W11501, doi:10.1029/2011WR010555.
- Xie, Y., C. T. Simmons, A. D. Werner, and H.-J. G. Diersch (2012), Prediction and uncertainty of free convection phenomena in porous media, *Water Resour. Res.*, *48*, W02535, doi:10.1029/2011WR011346.
- Yang, J., and R. N. Edwards (2000), Predicted groundwater circulation in fractured and unfractured anisotropic porous media driven by nuclear fuel waste heat generation, *Can. J. Earth Sci.*, *37*(9), 1301–1308.
- Yang, J., R. R. Large, and S. W. Bull (2004), Factors controlling free thermal convection in faults in sedimentary basins: Implications for the formation of zinc–lead mineral deposits, *Geofluids*, *4*(3), 237–247.
- Zhang, H., and F. W. Schwartz (1995), Multispecies contaminant plumes in variable density flow systems, *Water Resour. Res.*, *31*(4), 837–847, doi:10.1029/94WR02567.
- Zimmermann, S., P. Bauer, R. Held, W. Kinzelbach, and J. Walther (2006), Salt transport on islands in the Okavango Delta: Numerical investigations, *Adv. Water Resour.*, *29*(1), 11–29.
- Zoia, A., C. Latrille, A. Beccantini, and A. Cartalade (2009), Spatial and temporal features of dense contaminant transport: Experimental investigation and numerical modeling, *J. Contam. Hydrol.*, *109*, 14–26.